

## MEASUREMENTS OF DEEP INELASTIC SCATTERING AT HERA

MATTHEW WING

*Department of Physics and Astronomy, UCL  
Gower Street, London WC1E 6BT, UK  
E-mail: m.wing@ucl.ac.uk*

After fifteen years of running and a further five years of analysis, the final inclusive deep inelastic scattering cross sections from H1 and ZEUS have been published. Measurements of neutral current and charged current processes in  $ep$  collisions at HERA are presented. These provide us with the most valuable information on the structure of the proton, which tells us about the fundamental structure of matter and is essential for understanding processes at proton colliders such as the Large Hadron Collider. The measurements also demonstrate the chiral structure of the weak force and give a beautiful demonstration of the unification of the electromagnetic and weak forces. The new data will be presented in detail and comparisons with the latest predictions of the Standard Model shown. The H1 and ZEUS collaborations have also performed fits of the parton distribution functions in the proton; the results of these fits will also be presented.

### 1 Introduction

In this paper, measurements of deep inelastic  $ep$  scattering (DIS), at high virtualities,  $Q^2$ , of the exchanged boson, at HERA are presented. Both the H1 and ZEUS collaborations have recently published inclusive measurements for the full HERA data set of neutral and charge current DIS at high  $Q^2$  with incoming electrons or positrons of positive or negative polarisation. The neutral current reaction is mediated by a photon or a  $Z^0$  boson, dependent on the  $Q^2$  value, and the charge current reaction is mediated by  $W^\pm$  bosons. The data provide a probe of the electroweak structure of the Standard Model and in particular verify the unification of electromagnetism and the weak force at scales around the masses of the weak bosons and test the chiral nature of the electroweak force. The data also provide strong constraints on the structure of the proton allowing precise determinations of the parton density functions (PDFs) of the proton. This elucidates one of the most important questions in science, the structure of matter at its most fundamental level, and on a practical level provides crucial input to other facilities colliding protons such as the LHC. A final motivation for these measurements is that they probe the highest ever scales for  $ep$  scattering and so may elucidate new physical phenomena, such as quark substructure, or provide strong constraints on their existence.

The kinematic coverage of the HERA results, in  $Q^2$  and  $x$ , the fraction of the proton's momentum carried by the struck parton, is shown compared to fixed-target DIS experiments and  $pp/pp\bar{p}$  colliders in Fig. 1. This demonstrates that the HERA data overlap with both the low-energy DIS data and the high-energy hadron collider region. The results in these proceedings focus on the region above about

$Q^2 \sim 100 \text{ GeV}^2$  and so these data will constrain the parton densities in the region of overlap between HERA and LHC data. As the QCD evolution in  $Q^2$  is known, this then allows predictions of the parton densities at the much higher LHC energies to be made where there is no HERA data, but using the precise data shown here as input.

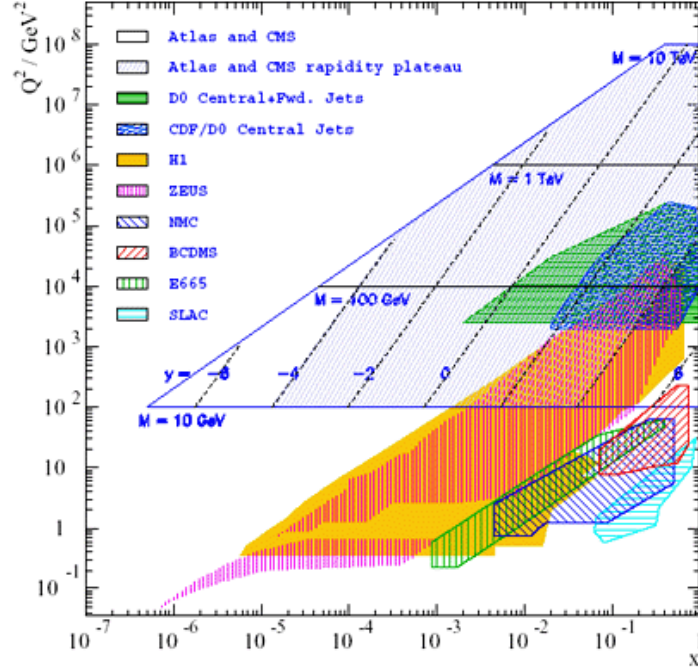


Figure 1. Kinematic coverage for DIS experiments and  $pp/pp\bar{p}$  colliders.

The unpolarised neutral current cross section can be written as

$$\frac{d^2\sigma_{\text{NC}}^{e^\pm p}}{dx dQ^2} = \frac{2\pi\alpha^2}{xQ^4} [Y_+ F_2 \mp Y_- xF_3 - y^2 F_L] \quad (1)$$

where  $\alpha$  is the fine structure constant,  $y$  is the inelasticity and is related to the other DIS variables by  $y = Q^2/(xs)$ , where  $s$  is the squared centre-of-mass energy and  $Y_\pm = 1 \pm (1 - y)^2$ . The structure functions represent the following:  $F_2$  is the sum of  $q$  and  $\bar{q}$  densities;  $xF_3$  is the density of valence quarks; and  $F_L$  is the gluon density which is important at high  $y$  and low  $Q^2$ .

The unpolarised charge current cross section can be written as

$$\frac{d^2\sigma_{\text{CC}}^{e^\pm p}}{dx dQ^2} = \frac{G_F^2}{2\pi} \frac{M_W^2}{Q^2 + M_W^2} \tilde{\sigma}^{e^\pm p} \quad (2)$$

where  $G_F$  is Fermi's constant and  $M_W$  is the mass of the  $W$  boson. The reduced cross section,  $\tilde{\sigma}$ , is sensitive to  $\bar{u}, \bar{c}$  and  $d, s$  quarks for  $e^+p$  data and to  $\bar{d}, \bar{s}$  and  $u, c$  quarks for  $e^-p$  data and so allows deconvolution of the quark densities which are just summed in  $F_2$ .

Inclusion of lepton polarisation modifies the above cross sections leading to sensitivity of for example the parity violating structure function,  $F_2^{\gamma Z}$ , and the couplings of the quarks to the  $Z$  boson. The physics and formulae will be discussed when presenting the appropriate results.

## 2 Experimental details

The HERA collider operated during 1992–2007 colliding electrons or positrons of 27.5 GeV with protons of (usually) 920 GeV giving a centre-of-mass energy of about 320 GeV. The period 1992–2000 is termed “HERA I” and the period 2002–2007, after the HERA and detector upgrades, is termed “HERA II”. Lower energy proton data was also taken during the early years of running and during the final period in order to measure the longitudinal proton structure function. Both H1 and ZEUS collected integrated luminosities of about  $0.5 \text{ fb}^{-1}$  each with roughly equal amounts of  $e^-p$  and  $e^+p$  data. The HERA II period represents about 75% of the data and during this period polarised lepton beams were delivered with roughly equal amounts of negative and positive polarisation (of magnitude 30%).

Example neutral and charge current events are shown in the detector displays in Fig. 2. As can be seen from the figure, the detectors are reasonably standard for high energy colliders with vertex detectors, tracking systems, calorimeters and muon detectors. In these representations, the electron enters the detector from the left and the proton enters from the right which is the reason for more instrumentation in the direction of the proton due to its much higher energy. The neutral current event shown in Fig. 2(a) has a clear signature of a scattered, high-energy, isolated electron back-to-back with a hadronic jet. The charge current event shown in Fig. 2(b) also has a hadronic jet but is balanced by a high-energy neutrino and so not observed in the detector and the missing energy is reconstructed from the kinematics. As the high-energy electron is a clearer signal than the reconstructed missing energy, the neutral current sample are generally more accurately reconstructed and have lower backgrounds than the charge current sample.

The results presented here focus on the completion of the analyses of the inclusive neutral and charge current data from the HERA II period in which data is taken with both negative and positive polarised electron and positron beams. The H1 Collaboration published all results in one extensive paper [1] whereas ZEUS published separately according to lepton running and process; the most recent discussed here are the neutral current [2] and charge current [3]  $e^+p$  data with the neutral current [4] and charge current [5]  $e^-p$  data published earlier.

As stated above, neutral current events are clean events which are accurately reconstructed via a variety of methods depending on the exact phase space or region of the detector. Examples of how well the data are reconstructed are shown in Fig. 3 where the scattered electron energy and angle of the hadronic system are compared to neutral current Monte Carlo simulation. All other variables are similarly well

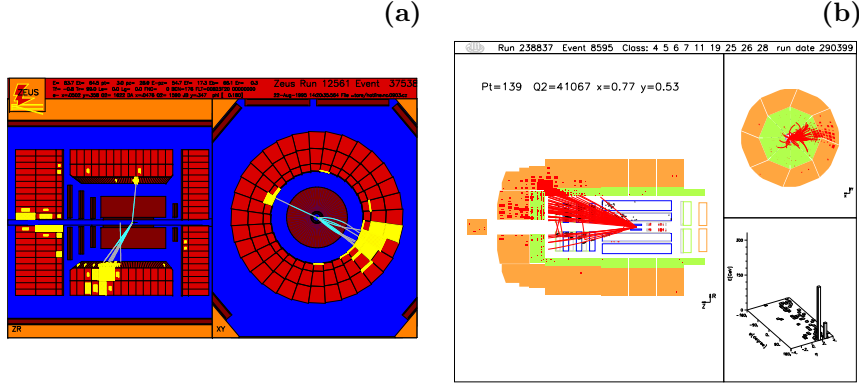


Figure 2. Event displays showing (a) a neutral current event in the ZEUS detector and (b) a charge current event in the H1 detector.

described and such control leads to a small systematic uncertainty of 1.5%.

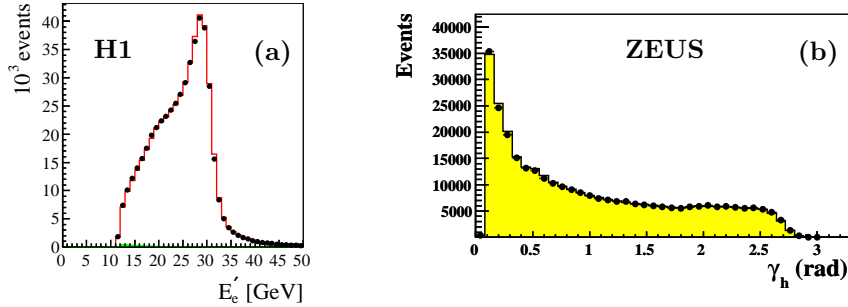


Figure 3. Example control plots for neutral current DIS events, (a) the electron energy,  $E'_e$ , and (b) the polar angle of the hadronic system,  $\gamma_h$ , for data (points) and Monte Carlo simulations of neutral current events (histogram). The background from primarily photoproduction is not visible on these scales.

In charge current events, the hadronic system and missing energy need to be well understood; the comparison of the Monte Carlo simulation with the data is shown in Fig. 4. Due to the missing energy, the description by the Monte Carlo is not as good as in neutral current events, but still under control. The background is also somewhat larger, but still small. The final systematic uncertainty is about 3%.

### 3 High- $Q^2$ electroweak physics

Measuring the neutral current and charge current cross sections over a wide range of  $Q^2$  and in particular at values up to  $M_{W,Z}^2$  allows the relationship to be investigated between the electromagnetic and weak interactions and, particularly due to

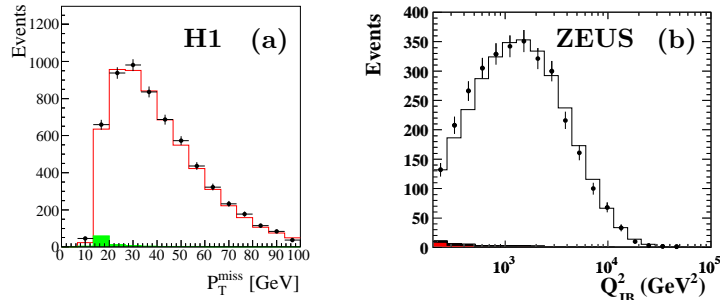


Figure 4. Example control plots for charge current DIS events, (a) the missing transverse momentum,  $P_T^{\text{miss}}$ , and (b) the exchanged boson virtuality reconstructed using the Jacquet–Blondel method,  $Q_{\text{JB}}^2$ , for data (points) and Monte Carlo simulations of charge current events (histogram). The background from primarily photoproduction is visible at low  $P_T^{\text{miss}}$  and low  $Q_{\text{JB}}^2$ .

using polarised electron and positron beams, understand the chiral structure of the electroweak interaction.

The  $Q^2$  dependence of the neutral and charge current unpolarised cross sections is shown in Fig. 5. At  $Q^2 \approx 200 \text{ GeV}^2$ , the neutral current cross section is over two orders of magnitude higher than the charge current cross section. Given the dependencies of the cross sections in Eqs. 1 and 2, the neutral current cross section initially falls much faster with increasing  $Q^2$  due to the dominance of photon exchange. The cross sections become of similar size and have a similar  $Q^2$  dependency at about  $10^4 \text{ GeV}^2$ . The equivalence of the photon and  $Z^0$  exchange in the neutral current process and the  $W^\pm$  exchange in the charge current process illustrate the unified behaviour of the electromagnetic and weak interactions.

The difference in the  $e^+p$  and  $e^-p$  unpolarised neutral current cross sections gives a direct measure of the structure-function  $xF_3^{\gamma Z}$ . Differences in the cross sections start for  $Q^2 > 1000 \text{ GeV}^2$  and increase with increasing  $Q^2$ . The extracted  $xF_3^{\gamma Z}$  is shown in Fig. 6 transformed to one value of  $Q^2$ ; the data are well described by predictions of the Standard Model using different proton PDFs.

Investigating the cross-section dependence on the lepton beam charge and polarisation reveals, in particular for the charge current process, a rich chiral structure. Figure 7 shows the strong dependence of the total charge current cross section on the lepton-beam polarisation and charge which is well described by Standard Model predictions. A linear fit to the data shows that the data are consistent with zero cross section when the positron beam has 100% negative polarisation and the electron beam has 100% positive polarisation. The results exclude the existence of charge current events involving right-handed fermions mediated by a boson of mass  $M_W^R$  below about  $200 \text{ GeV}$  assuming Standard Model couplings and a light right-handed  $\nu_e$ .

Although weaker than in charge current processes, the Standard Model also predicts a difference in the neutral current cross section for leptons of different helicity. A difference in the cross sections for negative and positive lepton polarisations has

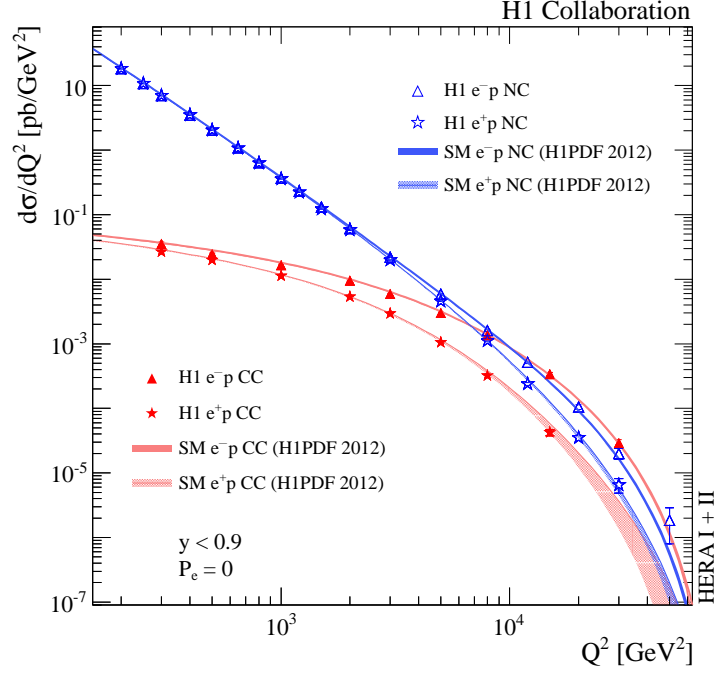


Figure 5. Differential cross-section  $d\sigma/dQ^2$  versus  $Q^2$  for neutral (open points) and charge (closed points) current data for the unpolarised  $e^-p$  (triangles) and  $e^+p$  (stars) data compared to Standard Model predictions.

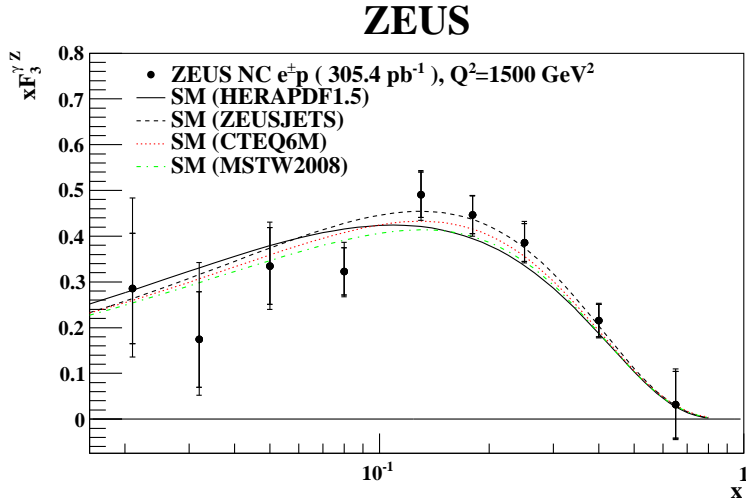


Figure 6. Structure-function  $xF_3^{\gamma Z}$  transformed to  $Q^2 = 1500 \text{ GeV}^2$  for data (points) and the Standard Model expectations from various sets of PDFs.

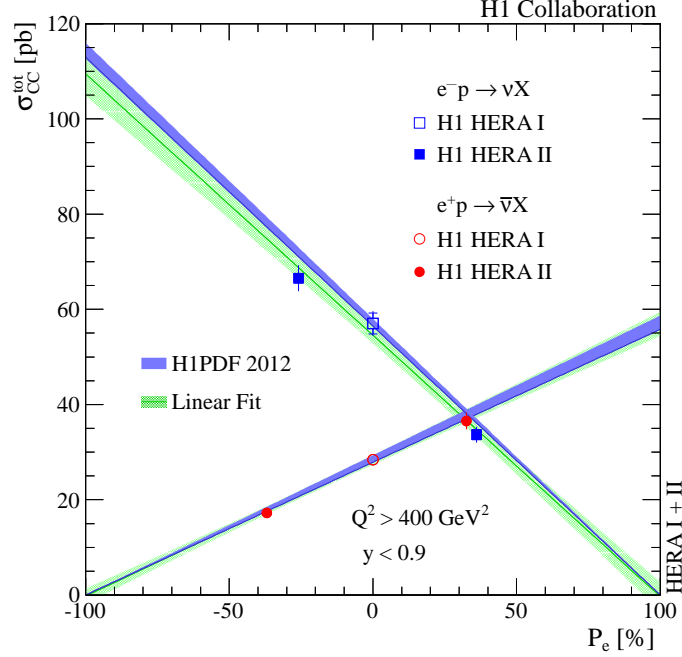


Figure 7. Dependence of the charge current cross section on polarisation of the electron-beam (squares) and positron-beam (circles) data. Predictions from the Standard Model (dark shaded band) and a linear fit to the data with its one standard deviation contour (line and light shaded band) are also shown.

been observed in the data, starting at about  $Q^2 > 1000 \text{ GeV}^2$  and increasing with increasing  $Q^2$ . The Standard Model predictions describe the data well and therefore the data confirm parity violation effects of the electroweak interaction. Using these high- $Q^2$  polarised neutral current data, the parity violating structure-function  $F_2^{\gamma Z}$  can be extracted for the first time. The difference of the  $e^+p$  and  $e^-p$  cross sections,  $(\sigma^\pm(P_L^\pm) - \sigma^\pm(P_R^\pm))/(\sigma^\pm(P_L^\pm) + \sigma^\pm(P_R^\pm))$ , where  $P_L^\pm$  and  $P_R^\pm$  are the negative and positive polarisations for  $e^\pm p$  data leads to the cancellation of the  $x F_3^Z$  and  $x F_3^{\gamma Z}$  terms and allows the direct extraction of  $F_2^{\gamma Z}$  [1]. The result is shown in Fig. 8 and is well described by theory.

Deconvolution of the different contributions to the charge current cross section can be seen in the reduced cross sections versus  $x$  at fixed  $Q^2$  and showing the Standard Model predictions separately for the quark flavour, e.g.  $x(\bar{u} + \bar{c})$  [1,3]. This can also be seen more strikingly by considering the dependence on the angular distribution of the scattered quark: in  $e^+q$  charged current DIS, the angular distribution will be flat in the positron-quark centre-of-mass scattering angle,  $\theta^*$ ; whereas it will exhibit a  $(1 + \cos \theta^*)^2$  distribution in  $e^+q$  scattering. Since  $(1 - y)^2 \propto (1 + \cos \theta^*)^2$ , the reduced cross section versus  $(1 - y)^2$  is shown, for fixed  $x$ , in Fig. 9. The data are well described by the Standard Model predictions. At leading order in QCD,

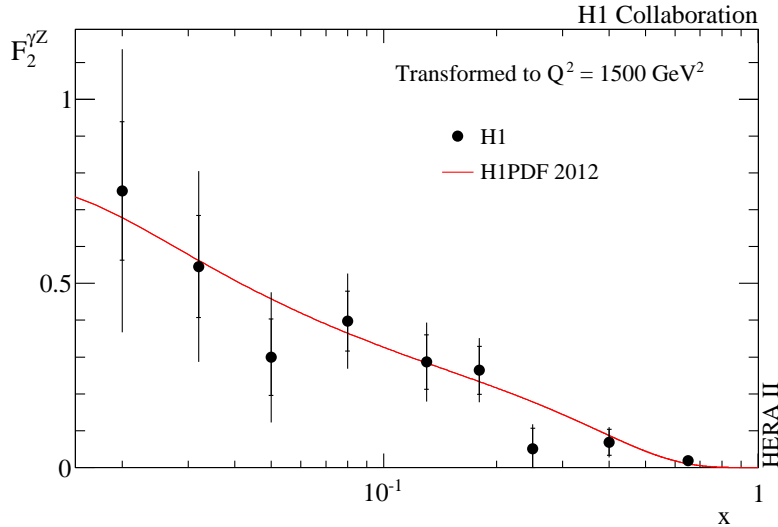


Figure 8. Structure-function  $F_2^{\gamma Z}$  transformed to  $Q^2 = 1500 \text{ GeV}^2$  for data (points) and the Standard Model expectation (line).

the intercept of the prediction gives the  $(\bar{u} + \bar{c})$  contribution, while the slope gives the  $(d + s)$  contribution.

As inclusive measurements of the DIS cross section provide data at the highest scales, they can be used to search for new high-energy phenomena such as leptoquarks [6,7] or quark substructure [8]. Given the incoming electron beam and quark from the proton, HERA provides a unique opportunity to search for resonantly-produced leptoquarks. Recently, both collaboration have published results on searches for leptoquarks in neutral and charge current events using the full data sample. An example “leptoquark” mass spectra is shown in Fig. 10 and compared to Standard Model predictions where a resonant-mass structure would be expected for leptoquark production. Given that neither experiment observed a significant deviation from the Standard Model, limits on the production of leptoquarks were extracted. Example results are presented in Fig. 10 in terms of limits on the Yukawa coupling,  $\lambda$ , as a function of  $M_{LQ}$  for a particular type of leptoquark ( $S_1^L$ ). The limits extend significantly beyond those from  $e^+e^-$  experiments and for high values of  $\lambda$  also extend up to higher masses than the results from the LHC where the results are independent of the coupling.

#### 4 Comparison to theory and extracted PDFs

Throughout the previous section the focus was on what can be learnt from considering the general theory of the Standard Model, although it was noted that the specific predictions incorporating electroweak and QCD effects describe the data well. In this section, the description of specific predictions is discussed and presented in more detail, in particular QCD fits to the data and the improvement in



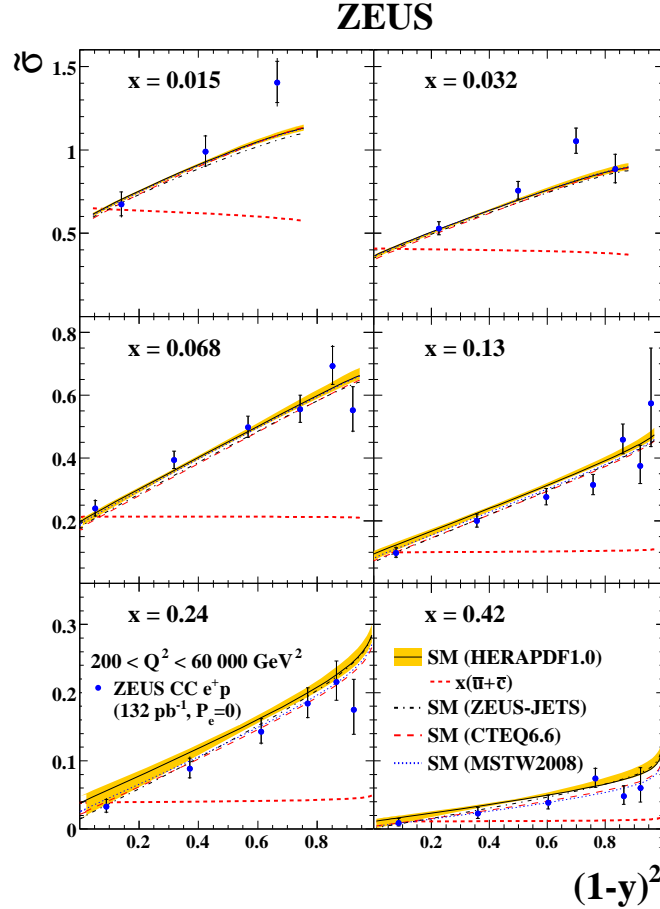


Figure 9. The  $e^+p$  charge current reduced cross section versus  $(1-y)^2$  for fixed  $x$  for data (points) and Standard Model predictions using different proton PDFs. The dashed lines show the PDF contribution  $x(\bar{u} + \bar{c})$ .

the proton PDFs using these data are presented.

The  $e^+p$  neutral current cross-section  $d\sigma/dQ^2$  is shown in Fig. 11 compared with Standard Model predictions using different protons PDFs, HERAPDF1.5 [10], ZEUSJETS [11], CTEQ6M [12] and MSTW2008 [13]. The HERAPDF1.5, ZEUSJETS and H1PDF2012 [1] (to be discussed in more detail) are extracted using their own respective data with a complete understanding of the correlations of the uncertainties. The CTEQ6M and MSTW2008 are global fits incorporating many additional different data sets such as from fixed-target DIS experiments, jet production at hadron colliders, etc.. These PDF fits used previous HERA data but not that shown in Fig. 11; the HERAPDF1.5 used all other ZEUS data and preliminary versions of the HERA II high- $Q^2$  data from H1. The predictions describe the data well over the seven orders of magnitude in the cross section.

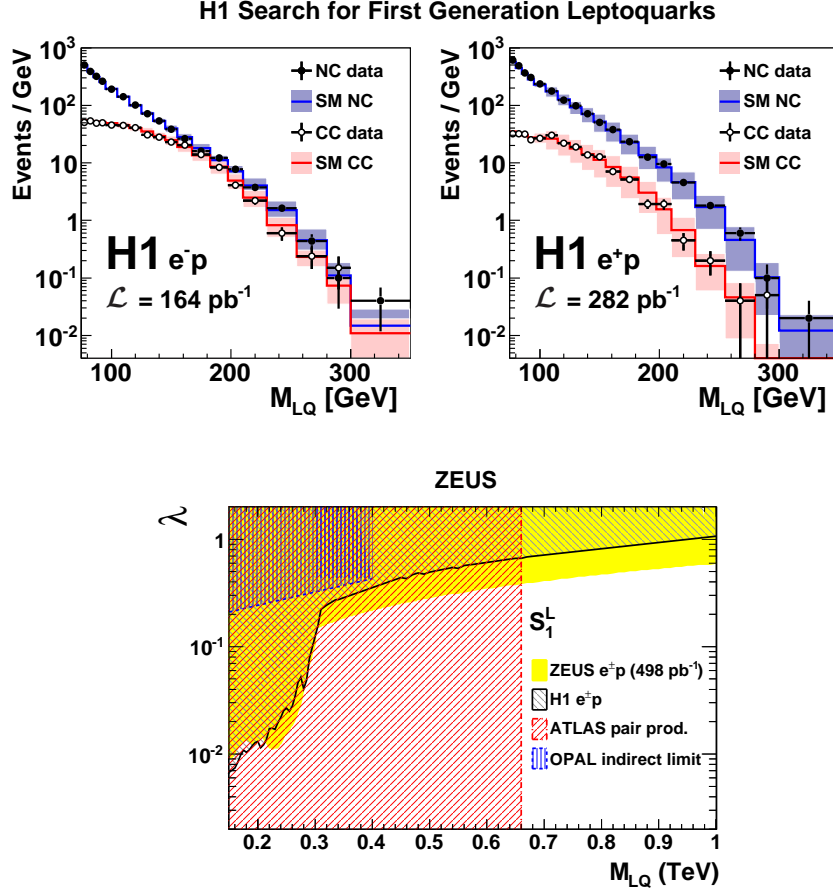


Figure 10. The neutral and charge current  $e^-p$  and  $e^+p$  data as a function of the leptoquark mass,  $M_{LQ} = \sqrt{Q^2/y}$ , compared to Standard Model predictions. Limits on the Yukawa coupling,  $\lambda$ , versus  $M_{LQ}$  showing HERA data compared to ATLAS  $pp$  and OPAL  $e^+e^-$  data.

The charge current data is similarly well described and the new data will be able to constrain the PDFs further.

The H1 Collaboration have done an NLO QCD fit to all their DIS data, H1PDF2012, also repeating the fit without the HERA II data to demonstrate the effect of the new data. The fit strategy follows closely that adopted for the determination of the HERAPDF1.0 sets and the reader is referred there [14] as well as the H1 publication [1] for more details. Simply put, the procedure relies on the factorisation of the DIS cross section into the short-distance cross section calculable in pQCD and the proton PDFs evolved with the  $Q^2$  by the DGLAP equations which are fit to the data. The fits are done in NLO QCD and also now NNLO QCD with a scale chosen as  $Q$  and assumptions such as the starting scale, the functional form of the individual PDFs, the heavy quark masses, etc. which are then varied to assess

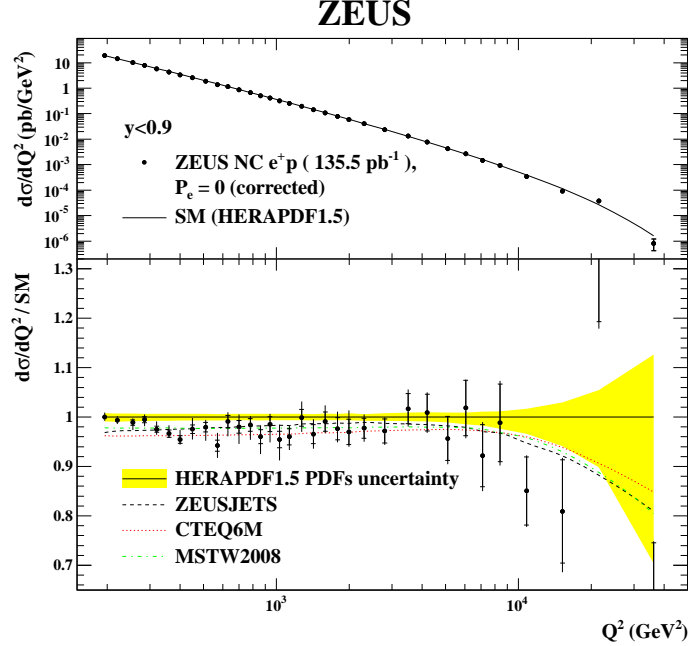


Figure 11. Neutral current cross-section  $d\sigma/dQ^2$  for unpolarised  $e^+p$  data (points) compared to the Standard Model with different choices of proton PDFs. The lower half shows the ratio of the data and other predictions to the Standard Model using the HERAPDF1.5.

the uncertainty on the procedure. The uncertainties consist of: the experimental which are derived from a change in  $\chi^2$  of 1 having taken into account correlations between data points and their uncertainties; model uncertainties which includes variations of the heavy-quark masses, minimum  $Q^2$  and strange-quark distribution; parameter uncertainties coming from an envelope corresponding to the set of fits in the  $\chi^2$  optimisation and from varying the starting scale.

The resulting  $\chi^2/\text{ndf}$  is about 1. Example PDFs and their uncertainties are shown evolved to  $Q^2 = M_W^2$  in Fig. 12. The valence quarks peak at about  $x = 0.1$  and dominate for high values whereas the gluon and sea-quark densities rise quickly with decreasing  $x$  and are over two orders of magnitude higher than the valence quark densities for  $x < 10^{-3}$ . Fitting different data sets separately or combined produced results in good agreement demonstrating the consistency of the data samples and fit procedure.

The relative uncertainties for the PDFs are shown in Fig. 13 for the combined fit and the fit to the HERA I data only. Inclusion of the HERA II data has an impact on all distributions, reducing the uncertainty by up to a factor of two, and particularly for the down-type quark distribution,  $xD$ . The impact of the HERA II data will also feed into any future HERAPDF version and global QCD fits.

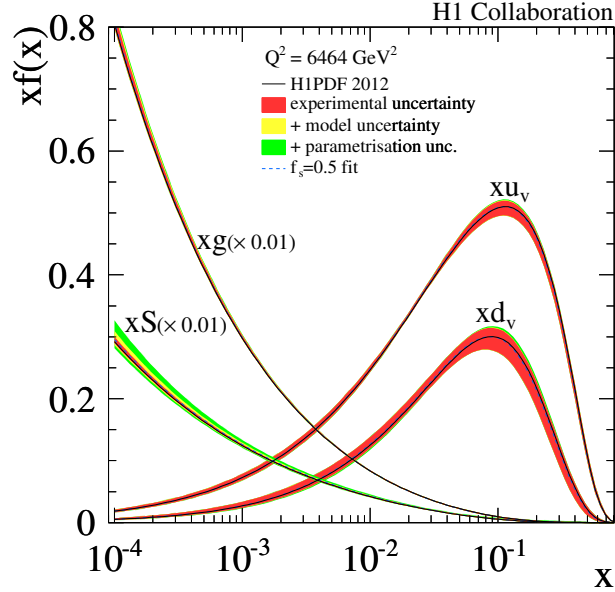


Figure 12. Parton distribution functions of H1PDF2012 at the scale of  $Q^2 = M_W^2 = 6464 \text{ GeV}^2$ . The gluon and sea distributions are scaled by a factor of 0.01. The PDFs with the strange quark fraction  $f_s = 0.5$  as found by ATLAS [9] are also shown.

## 5 HERAPDFs at the LHC

The HERAPDFs and global PDF fits are used extensively at the LHC such as in predictions of jet production, e.g. [15]. As shown in Fig. 14, all the various PDF fits give a similarly good description of the LHC data up to jet transverse energies of 1 TeV. That jet production at such high scales is so well and precisely predicted by the different PDF fits is due dominantly to the impact of the HERA data in these fits; the high  $Q^2$  data presented here will improve these predictions.

H1 and ZEUS have recently published a combined measurement of charm production in DIS [17]. As well as providing significantly improved results over any single measurement, it also has a significant impact constraining the charm mass and scheme used to calculate charm production in QCD fits. This then provides far more precise cross sections of  $W^\pm$  and  $Z^0$  production at the LHC.

The HERA data is crucial to many aspects of LHC physics and fits using all the high  $Q^2$  data shown here as well as the new charm results will be of great benefit to the LHC programme.

## 6 Summary

New, final results from both collaborations on the high- $Q^2$  neutral and charge current cross sections have been presented. They provide many beautiful demonstrations of our understanding of electroweak physics such as its chiral structure and

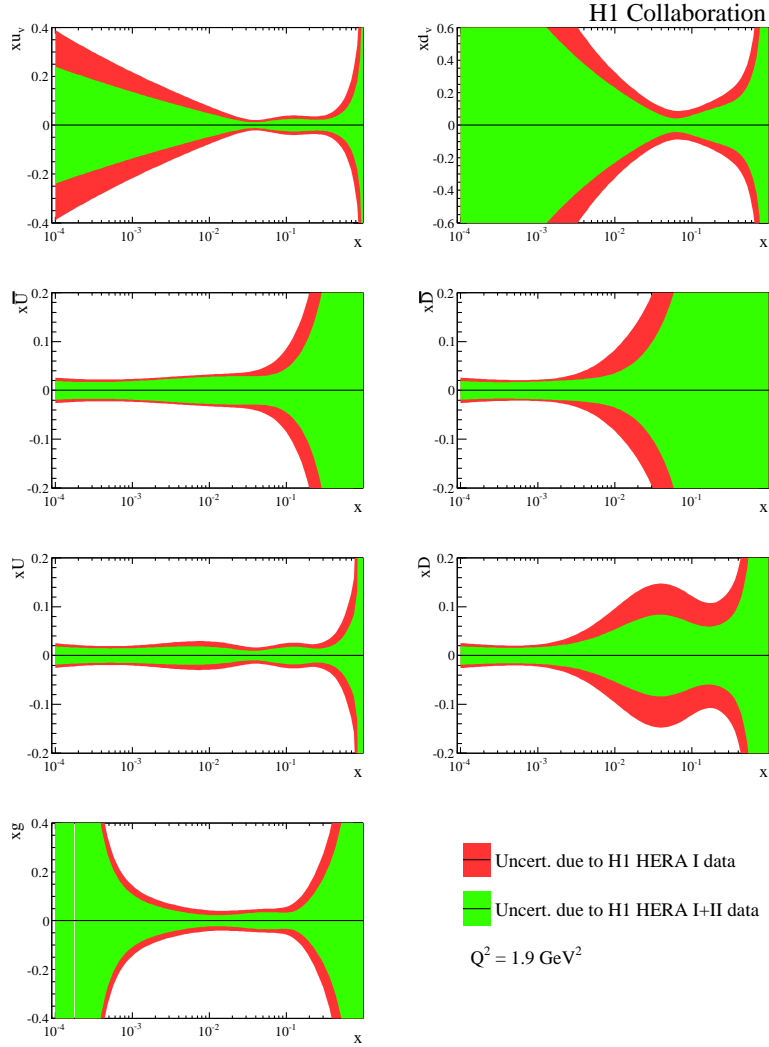


Figure 13. Comparison of relative experimental uncertainties of the PDFs extracted from HERA I (outer) and HERA II (inner) data under the same fit conditions.

the unification of electromagnetism and weak interactions. The data are precise and cover a wide kinematic range and along with the other HERA measurements provide the crucial constraints on the parton densities in the proton. In the future, the H1 and ZEUS high- $Q^2$  data will be combined and along with charm and jet data be used in HERAPDF fits.

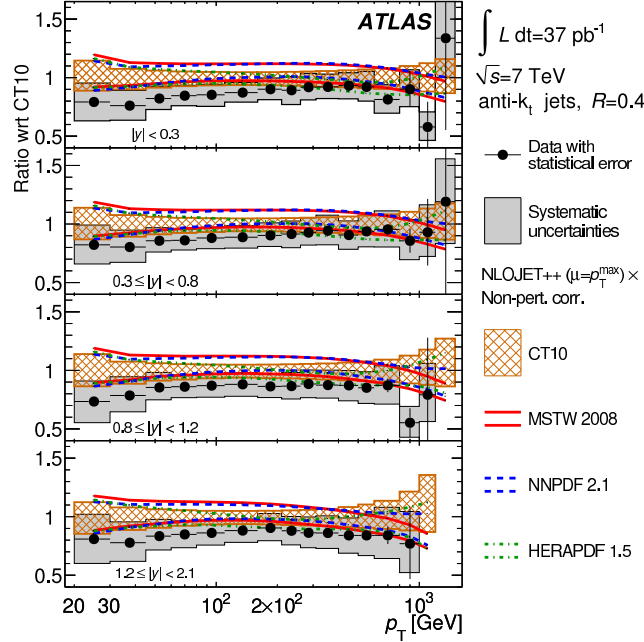


Figure 14. Ratios of inclusive jet double-differential, in transverse momentum and rapidity, cross sections to the CT10 PDF set [16] for ATLAS  $pp$  jet data (points) and different PDF sets.

## References

1. H1 Coll., F.D. Aaron et al., *JHEP* **09** (2012) 061.
2. ZEUS Coll, H. Abramowicz et al., DESY-12-145.
3. ZEUS Coll, H. Abramowicz et al., *Eur. Phys. J. C* **70** (2010) 945.
4. ZEUS Coll, H. Abramowicz et al., *Eur. Phys. J. C* **63** (2009) 171.
5. ZEUS Coll, H. Abramowicz et al., *Eur. Phys. J. C* **61** (2009) 223.
6. H1 Coll., F.D. Aaron et al., *Phys. Lett. B* **704** (2011) 388.
7. ZEUS Coll., H. Abramowicz et al., *Phys. Rev. D* **86** (2012) 012005.
8. H1 Coll., F.D. Aaron et al., *Phys. Lett. B* **705** (2011) 52.
9. ATLAS Coll., G. Aad et al., *Phys. Rev. Lett.* **109** (2012) 012001.
10. H1 and ZEUS Colls., *QCD NLO analysis of inclusive data (HERAPDF1.5)*, [https://www.desy.de/hizeus/combined\\_results/herapdf1.5/](https://www.desy.de/hizeus/combined_results/herapdf1.5/)
11. ZEUS Coll., S. Chekanov et al., *Eur. Phys. J. C* **42** (2005) 1.
12. J. Pumplin et al., *JHEP* **0207** (2002) 012.
13. A.D. Martin et al., *Eur. Phys. J. C* **63** (2009) 189.
14. H1 and ZEUS Colls., F.D. Aaron et al., *JHEP* **01** (2010) 109.
15. ATLAS Coll., G. Aad et al., *Phys. Rev. D* **86** (2012) 014022.
16. H.-L. Lai et al., *Phys. Rev. D* **82** (2010) 074024.
17. H1 and ZEUS Colls., F.D. Aaron et al., DESY-12-172.